



## [Mo<sub>3</sub>S<sub>13</sub>]<sup>2-</sup> modified TiO<sub>2</sub> coating on non-woven fabric for efficient photocatalytic mineralization of acetone



Yu Han<sup>a</sup>, Dongting Yue<sup>a</sup>, Miao Kan<sup>a</sup>, Yunwen Wu<sup>a</sup>, Jun Zeng<sup>b</sup>, Zhenfeng Bian<sup>c,\*</sup>, Yixin Zhao<sup>a</sup>, Xufang Qian<sup>a,\*</sup>

<sup>a</sup> School of Environmental Science and Engineering, Shanghai Jiao Tong University, 800 Dongchuan Road, Shanghai, 200240, China

<sup>b</sup> Key Laboratory of Green Chemistry of Sichuan Institutes of Higher Education, Sichuan University of Science & Engineering, China

<sup>c</sup> The Education Ministry Key Lab. of Resource Chemistry, Shanghai Key Laboratory of Rare Earth Functional Materials, Shanghai Normal University, Shanghai, 200234, China

### ARTICLE INFO

#### Keywords:

TiO<sub>2</sub>  
[Mo<sub>3</sub>S<sub>13</sub>]<sup>2-</sup>  
Photocatalytic oxidation  
Non-woven fabrics  
VOCs degradation

### ABSTRACT

Improving the photocatalytic efficiency of commercial TiO<sub>2</sub> has important significance for practical application of TiO<sub>2</sub> based photocatalysts. A novel photocatalyst [Mo<sub>3</sub>S<sub>13</sub>]<sup>2-</sup>/TiO<sub>2</sub> was fabricated by combining [Mo<sub>3</sub>S<sub>13</sub>]<sup>2-</sup> with commercial TiO<sub>2</sub> by an impregnation method. This composite photocatalyst presented a remarkable enhancement on photocatalytic mineralization of acetone in comparison with commercial TiO<sub>2</sub>. The optimum loading amount of [Mo<sub>3</sub>S<sub>13</sub>]<sup>2-</sup> was 1.7wt%, which is more efficient than the Pt/TiO<sub>2</sub> (1.5wt%). Electrochemical impedance spectroscopy (EIS) showed the smooth electron transfer pathway in [Mo<sub>3</sub>S<sub>13</sub>]<sup>2-</sup>/TiO<sub>2</sub> composite, facilitating the photo-charges separation during the photocatalysis process. Reactive oxygen species scavenging test illustrated that superoxide radical (·O<sub>2</sub><sup>-</sup>), hydroxyl radical (·OH) and photo-induced hole (h<sup>+</sup>) were all contributing to the acetone degradation. The [Mo<sub>3</sub>S<sub>13</sub>]<sup>2-</sup>/TiO<sub>2</sub> photocatalyst was deposited on non-woven fabrics which showed obvious promotion on the photocatalytic degradation of acetone in comparison with pristine commercial TiO<sub>2</sub>.

### 1. Introduction

People spend about 80% of their life indoors and the United States Environmental Protection Agency reported that indoor air is two to five more polluted than outdoor air [1,2]. Volatile and semi-volatile organic compounds are the dominating hazardous pollutants in the indoor and enclosed space, such as households, industrial areas, laboratories and office building [3–5]. As a green and environmental-friendly method, semiconductor photocatalytic oxidation has been widely investigated [6–12]. TiO<sub>2</sub> as one of the photocatalysts draw a mass of attention due to its excellent photocatalytic efficiency, high stability and low cost in degrading organic pollutants [5,10,11].

Whereas, the limited utilization of photo-induced carriers, electrons (e<sup>-</sup>) and holes (h<sup>+</sup>), suspends the practical application of TiO<sub>2</sub>. The conduction band (CB) e<sup>-</sup> transfer to oxygen molecule existing ubiquitously in the photocatalysis systems has been considered as the rate-determining step in semiconductor photocatalysis [13,14]. The slow interfacial electrons transfer was the primary reason for the less utilization of photo-induced charges [15,16]. As co-catalysts can capture and transfer the electrons efficiently and improve the charge

separation, co-catalysts are extensively used to ameliorate the photocatalytic activities of photocatalysts [14,8–18]. Pt, Ag and other noble metal were reported massively as the co-catalysts to improve the photocatalytic efficiency [19–21]. However, the high cost and the scarcity limited the large-scale application of noble-metal co-catalysts. Thus, non-noble metal as the co-catalysts drawn numerous attentions. As one of the most widely investigated non-noble metal co-catalysts, MoS<sub>2</sub> has shown an excellent performance in photocatalysis and electrocatalysis [22–25]. Besides of MoS<sub>2</sub>, other molybdenum sulfides have also been identified as promising co-catalysts. Among them, thiomolybdate [Mo<sub>3</sub>S<sub>13</sub>]<sup>2-</sup> contains three different types of sulfur ligands, which all resemble the active edge site of MoS<sub>2</sub>. It has been reported that the unique molecule structure of [Mo<sub>3</sub>S<sub>13</sub>]<sup>2-</sup> prominently facilitated the effective H<sub>2</sub> evolution in the hydrogen-evolution reaction (HER) [26–29]. However, to the best of our knowledge, there is no report about [Mo<sub>3</sub>S<sub>13</sub>]<sup>2-</sup> modifying TiO<sub>2</sub> to study the photocatalytic properties in VOCs mineralization. In this paper, we used acetone as the model VOCs which is abundant in the cabins [30,31]. Our results indicated that [Mo<sub>3</sub>S<sub>13</sub>]<sup>2-</sup> displayed excellent performance doubling the photocatalytic activity compared to the commercial TiO<sub>2</sub> (P25). The

\* Corresponding authors.

E-mail addresses: [bianzhenfeng@shnu.edu.cn](mailto:bianzhenfeng@shnu.edu.cn) (Z. Bian), [qianxufang@sjtu.edu.cn](mailto:qianxufang@sjtu.edu.cn) (X. Qian).

predominant oxidant species during the photocatalysis process were also detected and discussed. Additionally, the photocatalysts were deposited on polypropylene non-woven fabric which is lightweight, antibacterial and low cost [32–34]. The  $[Mo_3S_{13}]^{2-}/TiO_2$  deposited non-woven fabric maintained the same increment on photocatalytic mineralization activity in comparison with pristine  $TiO_2$ /fabric.

## 2. Experimental

### 2.1. Chemicals

$TiO_2$  powders (Degussa P25, ca. 80% anatase) were used as received. Non-woven 100% polypropylene fabric ( $65.3\text{ g/m}^2$ ) in white color was used as the substrate. Ammonium heptamolybdate tetrahydrate ( $(NH_4)_2Mo_7O_{24} \cdot 4H_2O$ ), carbon disulfide, silicon dioxide, chloroplatinic acid hexahydrate, ethanol, acetone, *p*-benzoquinone, and toluene was of analytical purity and used as received. All of them were purchased from Sinopharm Chemical Reagent Co., Ltd. Ammonium polysulfide solution was purchased from Xiya reagent. Barium sulfate was purchased from Aladdin Industrial Corporation. Potassium iodide (KI) was purchased from Shanghai Macklin Biochemical Co., Ltd. Coumarin was purchased from J&K Scientific Ltd.

### 2.2. Materials synthesis

#### 2.2.1. Preparation of $[Mo_3S_{13}]^{2-}/TiO_2$ and $Pt/TiO_2$

The thiomolybdate  $(NH_4)_2Mo_7O_{24} \cdot nH_2O$  ( $n = 0-2$ ) was prepared according to the literature [29]. The  $[Mo_3S_{13}]^{2-}$  was immobilized on  $TiO_2$  by an impregnation method. In a typical process, different amounts of  $[Mo_3S_{13}]^{2-}$  solution was dispersed in the ethanol (30 mL,  $\geq 99.5\%$ ) to obtain a uniform mixture solution. Then 150 mg of  $TiO_2$  powder (Degussa P25, ca. 80% anatase) were dispersed into the above mixture solution by sonification. The weight contents of  $[Mo_3S_{13}]^{2-}$  in the composites photocatalysts were adjusted from 0.6 wt%, 1.1 wt%, 1.7 wt% to 3.4 wt%. The suspension was stirred for 4.5 h before being centrifuged and washed. The  $[Mo_3S_{13}]^{2-}/TiO_2$  composites were washed by affluent amounts of deionized water and ethanol before drying in a vacuum oven at  $40^\circ\text{C}$  overnight. The  $[Mo_3S_{13}]^{2-}/TiO_2$  composites were designated as 0.6 $[Mo_3S_{13}]^{2-}/TiO_2$ , 1.1 $[Mo_3S_{13}]^{2-}/TiO_2$ , 1.7 $[Mo_3S_{13}]^{2-}/TiO_2$  and 3.4 $[Mo_3S_{13}]^{2-}/TiO_2$ . For comparison,  $Pt/TiO_2$  photocatalysts with  $Pt$  of 1.5 wt% were synthesized according to the previous report [35].

#### 2.2.2. $[Mo_3S_{13}]^{2-}/TiO_2$ photocatalysts coating on polypropylene non-woven fabrics

Different amounts (30 mg, 40 mg, 50 mg) of  $[Mo_3S_{13}]^{2-}/TiO_2$  photocatalysts were dissolved in 5 mL ethanol to obtain uniform suspensions. The obtained suspensions kept uniformly before being sprayed onto non-woven polypropylene fabric (area =  $36\text{ cm}^2$  and  $0.25\text{ m}^2$ ) via an airbrush (U-STAR S-130) (Fig. S1). The supply gas pressure was controlled as 0.1 MPa. The treated fabrics were dried in a vacuum oven at  $60^\circ\text{C}$  overnight. For comparison, the pristine  $TiO_2$  particle was also loaded on the fabrics in the same way.

### 2.3. Characterization

X-ray diffraction analysis of the as-prepared samples were carried out on Shimadzu XRD-6100 diffractometer with  $Cu K\alpha$  radiation ( $\lambda = 1.54\text{ \AA}$ ). The data were recorded at a scan rate of  $5^\circ/\text{min}$  in the  $2\theta$  range from  $10^\circ$  to  $80^\circ$ . UV-vis diffuse reflectance spectra (UV-vis DRS) were measured on UV-vis spectrophotometer (Shimadzu UV-2450, Japan). The elemental composition of the composites was determined by inductively coupled plasma optical emission spectrometer (ICP-AES, iCAP6300, Thermo, USA). The morphologies of samples were characterized with field emission scanning electron microscope (FESEM) (FEI & Oxford Sirion 200) and Transmission electron microscopy (TEM)

(JEOL-JEM-2010, Japan) employing a 200 kV accelerating voltage. X-ray photoelectron spectroscopy (XPS) (AXIS Ultra DLD Kratos, Japan) analysis was carried out to study the surface electronic states of the samples. All binding energies were calibrated by the C 1s peaks of the surface adventitious carbon (284.6 eV). Fourier transform infrared (FTIR) spectra of the samples were measured on Tensor 27 FTIR spectrometer (Nicolet 6700). The surface physical adsorption property was studied through the contact angle (CA), which were measured using the sessile droplet method with a contact angle meter (KRUESS GmbH, Germany). The value of the contact angle was the average of five measurements on a sample. The electrochemical measurement was conducted in a three-electrodes system, where Pt plate as the counter electrode, Ag/AgCl electrode as the reference electrode and 1.0 M perchloric acid as the electrolyte, on ZAHNER PP211 electrochemical workstation. The working electrode was prepared by spreading 5  $\mu\text{L}$  slurry on fluorine tin oxide (FTO) glass. The slurry contained 0.2 mL deionized water, 0.8 mL ethanol 100  $\mu\text{L}$  Nafion and 2 mg sample. The obtained glass was dried at room temperature overnight.

### 2.4. Photocatalytic activity evaluation

In order to evaluate the photocatalytic activity of as-synthesized  $[Mo_3S_{13}]^{2-}/TiO_2$  composites, photocatalytic degradation of acetone was performed under a 300 W Xe arc lamp (21 A imported current, through a  $50 \times 50\text{ mm}$  aperture winder). A 20 mg of as-prepared photocatalysts and 480 mg of  $SiO_2$  were milled homogeneously before spreading evenly on a glass fiber plate (area of mixed powder,  $16\text{ cm}^2$ ). In reactive oxygen species experiment, 2 mg scavenger was added into the mixture of photocatalysts and  $SiO_2$  before milling. The vessel was pretreated by  $O_2$  for 30 min to create an oxygen-rich environment. Then the acetone (6  $\mu\text{L}$ ) was injected into the vessel. After ensuring the sufficient mixture of gas in the closed vessel, the reactor was placed under the light irradiation. Every 30 min, a certain volume (500  $\mu\text{L}$ ) gas extracted from the vessel was injected into the gas chromatograph (GC-7900 equipped with a methane reforming furnace and flame ionization detector (FID)).

## 3. Results and discussion

The  $[Mo_3S_{13}]^{2-}/TiO_2$  composites with different mass ratios were synthesized through an impregnation method. The XRD patterns of pristine  $TiO_2$  and  $[Mo_3S_{13}]^{2-}/TiO_2$  composites showed the typical characteristic diffraction peaks of  $TiO_2$  containing anatase and rutile (Fig. 1). None of the newly appeared diffraction peaks assigning to  $[Mo_3S_{13}]^{2-}$  were found on  $[Mo_3S_{13}]^{2-}/TiO_2$  nanocomposites indicating that the high dispersed loading of  $[Mo_3S_{13}]^{2-}$  [6].

TEM analysis was carried out to investigate the crystal structure and the composition of the composites (1.7 $[Mo_3S_{13}]^{2-}/TiO_2$ ). As shown in

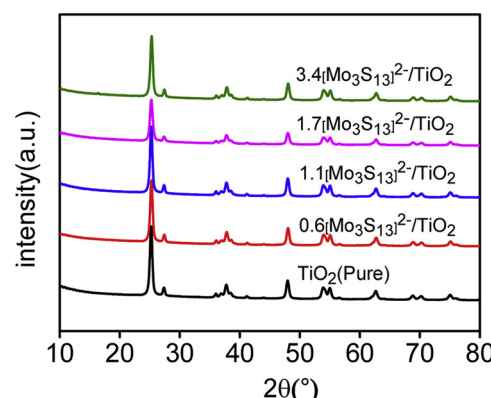


Fig. 1. XRD patterns of  $TiO_2$  and  $[Mo_3S_{13}]^{2-}/TiO_2$  composites with different contents of  $[Mo_3S_{13}]^{2-}$ .

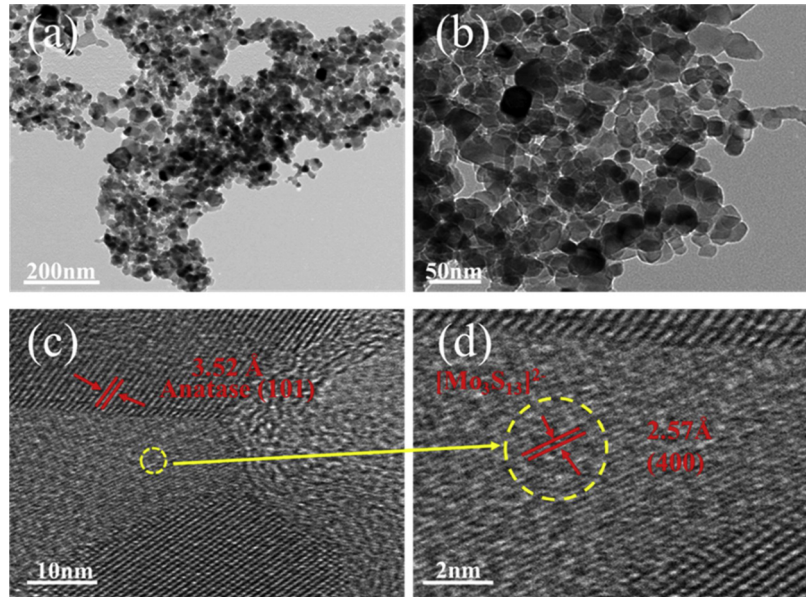


Fig. 2. TEM images and HRTEM images of  $1.7[\text{Mo}_3\text{S}_{13}]^{2-}/\text{TiO}_2$  composites.

**Fig. 2a** and **b**, the P25 photocatalyst is composed of nanoparticles with the diameter of around 25 nm. High-resolution TEM (HRTEM) images were shown in **Fig. 2c** and **d**. The fringe spacing of 0.352 nm was consistent with the interplanar spacing (0.351 nm) of (101) lattice planes of anatase  $\text{TiO}_2$  (**Fig. 2(c)**). The interplanar spacing of  $[\text{Mo}_3\text{S}_{13}]^{2-}$  was 0.257 nm (**Fig. 2(d)**), which is consistent with previous reports [28]. The results demonstrated the  $[\text{Mo}_3\text{S}_{13}]^{2-}$  had been successfully deposited on the  $\text{TiO}_2$  nanoparticles surface by the impregnation method.

XPS spectrum of Ti 2p for pristine  $\text{TiO}_2$  emerged at 458.26 eV and 464.06 eV corresponded with  $\text{Ti}2\text{p }3/2$  and  $\text{Ti}2\text{p }1/2$ , which illustrated the  $\text{Ti}^{4+}$  oxidation state of  $\text{TiO}_2$  (**Fig. 3(a)**) [36,37]. Whereas, the peaks of binding energy of Ti 2p in the synthetic composites,  $1.7[\text{Mo}_3\text{S}_{13}]^{2-}/\text{TiO}_2$ , altered slightly, locating at 458.33 eV and 463.93 eV, respectively. The spin-orbital splitting of  $\text{Ti}2\text{p }3/2$  and  $\text{Ti}2\text{p }1/2$  in the  $1.7[\text{Mo}_3\text{S}_{13}]^{2-}/\text{TiO}_2$  was 5.6 eV, which was smaller than that of pristine  $\text{TiO}_2$  (5.8 eV). The results should be ascribed to the successful doping of  $[\text{Mo}_3\text{S}_{13}]^{2-}$  on the  $\text{TiO}_2$  and implied the interaction between  $[\text{Mo}_3\text{S}_{13}]^{2-}$  and  $\text{TiO}_2$  were not simply physical adsorption [5,6]. To confirm the existence of  $[\text{Mo}_3\text{S}_{13}]^{2-}$ , we also gave the XPS spectra of Mo 3d and S 2p. The characteristic peaks of Mo (**Fig. 3(b)**) were presented at 231.3 eV and 233.9 eV, which are attributed to the binding energy of  $\text{Mo}3\text{d }5/2$  and  $\text{Mo}3\text{d }3/2$  orbits with +4 oxidation state, respectively. This result was consistent with our previous research [6]. The S 2p spectrum (**Fig. S2**) was also consistent with previous reports [38,39]. FTIR spectrum (**Fig. S3**) of  $\text{TiO}_2$  revealed three characteristic peaks at 3438, 1637, 659  $\text{cm}^{-1}$  assigned to stretching vibration of

hydroxyl groups, bending vibration of surface O–H group and Ti–O–Ti bridging stretching mode, respectively [40,41]. Whereas, one new peak at  $1384 \text{ cm}^{-1}$  appeared in the FTIR spectrum of  $[\text{Mo}_3\text{S}_{13}]^{2-}/\text{TiO}_2$ , which was associated to Mo–S bonding [39,42].

The gas-solid photocatalytic oxidation of acetone was studied over the  $[\text{Mo}_3\text{S}_{13}]^{2-}/\text{TiO}_2$  composites and pristine  $\text{TiO}_2$  by evaluating the  $\text{CO}_2$  production under UV-vis light irradiation. **Fig. 4(a)** presented the  $\text{CO}_2$  production curve as a function of time.  $\text{CO}_2$  was not generated without the UV-vis light irradiation or the photocatalysts, which was demonstrated by the blank experiment in **Figs. 4** and **S4**. In the presence of pristine  $\text{TiO}_2$ , the  $\text{CO}_2$  production curve showed linear tendency and  $49.3 \mu\text{mol}$   $\text{CO}_2$  was detected after 90 min irradiation. The deposition of  $[\text{Mo}_3\text{S}_{13}]^{2-}$  on  $\text{TiO}_2$  improves the degradation of acetone and  $\text{CO}_2$  production. The  $\text{CO}_2$  production after 90 min irradiation was  $65.4 \mu\text{mol}$ ,  $77.0 \mu\text{mol}$ ,  $107.5 \mu\text{mol}$  and  $60.9 \mu\text{mol}$  for  $0.6[\text{Mo}_3\text{S}_{13}]^{2-}/\text{TiO}_2$ ,  $1.1[\text{Mo}_3\text{S}_{13}]^{2-}/\text{TiO}_2$ ,  $1.7[\text{Mo}_3\text{S}_{13}]^{2-}/\text{TiO}_2$  and  $3.4[\text{Mo}_3\text{S}_{13}]^{2-}/\text{TiO}_2$  composites, respectively. The results indicated that the optimal loading amount of  $[\text{Mo}_3\text{S}_{13}]^{2-}$  is 1.7 wt%. It has been reported that  $[\text{Mo}_3\text{S}_{13}]^{2-}$  also greatly enhanced the electrocatalytic  $\text{H}_2$  production for graphite paper, which indicates the electron capture capability of co-catalysts  $[\text{Mo}_3\text{S}_{13}]^{2-}$  [43]. Pt nanoparticles was an efficient co-catalyst in photocatalysis. Falch et al. reported that the optimal amount of Pt was 1.5 wt% in hydrogen production system [35]. Here we compared the  $\text{CO}_2$  production process under the presence of  $1.7[\text{Mo}_3\text{S}_{13}]^{2-}/\text{TiO}_2$  with that of  $1.5 \text{ Pt}/\text{TiO}_2$ . After 90 min irradiation,  $84.4 \mu\text{mol}$   $\text{CO}_2$  was detected which is less than that produced on  $1.7[\text{Mo}_3\text{S}_{13}]^{2-}/\text{TiO}_2$ . The above results supported that  $[\text{Mo}_3\text{S}_{13}]^{2-}$  would become a satisfying

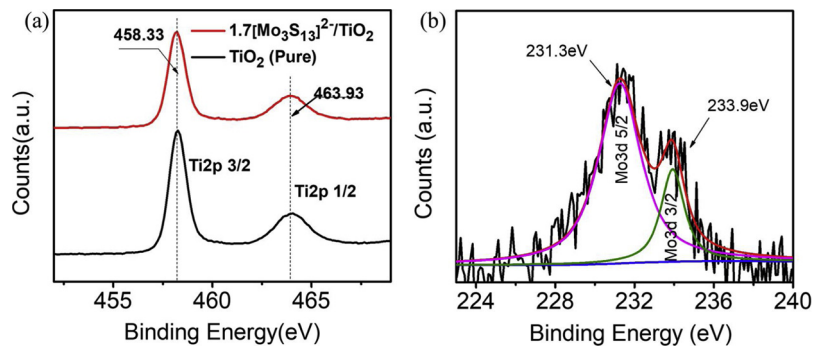
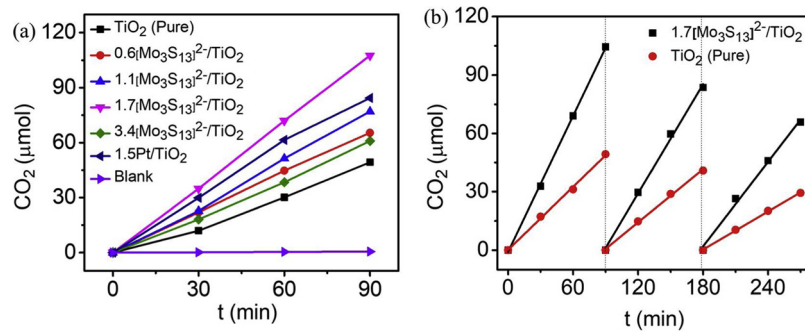


Fig. 3. XPS spectra of Ti 2p (a) and Mo 3d (b) of pure  $\text{TiO}_2$  and the  $1.7[\text{Mo}_3\text{S}_{13}]^{2-}/\text{TiO}_2$  composites.



**Fig. 4.** (a) CO<sub>2</sub> production on different catalysts during the photocatalytic degrading of acetone; (b) CO<sub>2</sub> production in cycle runs of photocatalytic degradation of acetone.

alternative to noble metal co-catalyst, such as Pt. We also compared the photocatalytic degradation efficiency between [Mo<sub>3</sub>S<sub>13</sub>]<sup>2-</sup>/TiO<sub>2</sub> composite and some other reported photocatalysts. [Mo<sub>3</sub>S<sub>13</sub>]<sup>2-</sup>/TiO<sub>2</sub> composite simultaneously had high CO<sub>2</sub> initial production rate and high acetone mineralization ratio (Table S1). In addition, [Mo<sub>3</sub>S<sub>13</sub>]<sup>2-</sup>/TiO<sub>2</sub> composite photocatalysts presented a hump-like variation tendency on photocatalytic activity relying on the loading amount of [Mo<sub>3</sub>S<sub>13</sub>]<sup>2-</sup>. The ascent stage as the increasing loading amount was ascribed to that [Mo<sub>3</sub>S<sub>13</sub>]<sup>2-</sup> could facilitate the separation of photo-charges. The decline stage along with the increasing loading amount was due to that excess loading would shade the surface of TiO<sub>2</sub>, which suppressed the light absorption of photocarrier. The stability of composite photocatalysts was investigated by the cycling life test. As Fig. 4(b) shown, the initial reaction rates of the three cycles on the 1.7[Mo<sub>3</sub>S<sub>13</sub>]<sup>2-</sup>/TiO<sub>2</sub> test were 1.16 μmol/min, 0.94 μmol/min, 0.72 μmol/min, respectively. The initial reaction rate fell down about 37.9% in the third run. We also measured the initial reaction rates of the three cycles on the 1.1[Mo<sub>3</sub>S<sub>13</sub>]<sup>2-</sup>/TiO<sub>2</sub>. The initial reaction rate fell down about 34.5% in the third run (Fig. S5). The cycling stability of the pristine TiO<sub>2</sub> was measured for comparison. The initial reaction rates were 0.58 μmol/min, 0.49 μmol/min, 0.35 μmol/min, respectively. The initial reaction rate fell down about 39.6% in the third run. The decay rates of initial reaction rate between [Mo<sub>3</sub>S<sub>13</sub>]<sup>2-</sup>/TiO<sub>2</sub> composites and pristine TiO<sub>2</sub> were almost the same. Our previous work indicated [Mo<sub>3</sub>S<sub>13</sub>]<sup>2-</sup> nanoclusters were intrinsically stable under the UV-vis irradiation [44]. Thus, the similar decay rates of initial reaction rate between [Mo<sub>3</sub>S<sub>13</sub>]<sup>2-</sup>/TiO<sub>2</sub> composites and pristine TiO<sub>2</sub> should be ascribed to the accumulation of intermediate product on TiO<sub>2</sub> [45,46].

The optical properties of pristine TiO<sub>2</sub> and the [Mo<sub>3</sub>S<sub>13</sub>]<sup>2-</sup>/TiO<sub>2</sub> composites were studied by UV-vis diffuse reflectance spectra (DRS). The light absorptions of photocatalysts increased obviously due to the coating of [Mo<sub>3</sub>S<sub>13</sub>]<sup>2-</sup> clusters with brown color (Fig. S6). To figure out the reason for the improved photocatalytic activity, the electrochemical impedance spectroscopy (EIS) was carried out, which is usually used to understand the internal electron transfer process [9,47]. The diameter of the semicircle in correlation with the charge-transfer resistance of the electrode is smaller for [Mo<sub>3</sub>S<sub>13</sub>]<sup>2-</sup>/TiO<sub>2</sub> composite than that of

pristine TiO<sub>2</sub> in the high-frequency region (Fig. 5(a)), which should be attributed to [Mo<sub>3</sub>S<sub>13</sub>]<sup>2-</sup>/TiO<sub>2</sub> composite with good electrical conductivity indicating the smooth electron transfer pathway in [Mo<sub>3</sub>S<sub>13</sub>]<sup>2-</sup>/TiO<sub>2</sub> composite. Accordingly, the photo-induced charges separation efficiency was improved exceedingly, which benefited to the photocatalytic oxidation process. In addition, the polarization curves (Fig. S7) also indicated the efficient electrons transfer in composites [27].

The reactive oxygen species are the key points in the photocatalytic oxidation degradation. To understand the reaction mechanism in the degradation process, *p*-benzoquinone and KI were added into the reaction system as the superoxide radical (·O<sub>2</sub><sup>-</sup>) scavenger and photo-induced hole (h<sup>+</sup>) scavenger, respectively. As the Fig. 5(b) shown, the production of CO<sub>2</sub> was completely depressed when *p*-benzoquinone was added, indicating that ·O<sub>2</sub><sup>-</sup> was the vital reactive species in this degradation system. The photo-induced electrons in the conduction band were transferred fleetly through [Mo<sub>3</sub>S<sub>13</sub>]<sup>2-</sup> and reacted with O<sub>2</sub> absorbed in the surface of [Mo<sub>3</sub>S<sub>13</sub>]<sup>2-</sup>/TiO<sub>2</sub> composites to form ·O<sub>2</sub><sup>-</sup>, which could further oxidize organic compounds. Photo-induced holes also participated in the oxidation degradation process, according to the depressed production of CO<sub>2</sub> when KI was added. The holes (h<sup>+</sup>), which have high oxidation potential, could oxidize directly the adsorbed compounds [6]. Besides of this route to contribute in the degradation process, h<sup>+</sup> (E<sub>VB</sub> = 2.69 V at pH 7) could also react with the OH reactive site (E°(H<sub>2</sub>O/OH) = 2.29 V) (e.g. H-bonded OH, terminal Ti—OH and Ti—OH—Ti bridged) [11,48] on the TiO<sub>2</sub> to form the higher oxidation potential species hydroxyl radical (·OH), which participated in the photo-degradation process [49,50]. Specific signal molecule, coumarin could react with ·OH to form 7-hydrocoumarin, a strongly luminescent compound [51]. The fluorescence emission at 396 nm increased illustrating the production of 7-hydrocoumarin (Fig. S8). This result provided the evidence that ·OH was formed and participated in the process of mineralization of acetone (Fig. 6).

When the vessel was filled with Ar, there is no generated CO<sub>2</sub> could be detected. This phenomenon confirmed that O<sub>2</sub> is indispensable in photocatalytic degradation of gaseous pollutants as the electron acceptor. In the dry anaerobic atmosphere (Relative Humidity < 10%),

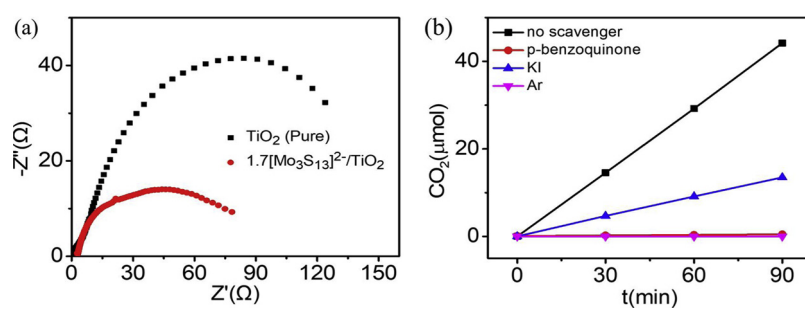


**Fig. 5.** (a) Nyquist plots of pristine TiO<sub>2</sub> and 1.7[Mo<sub>3</sub>S<sub>13</sub>]<sup>2-</sup>/TiO<sub>2</sub> composites; (b) CO<sub>2</sub> production with different reactive-species scavengers.

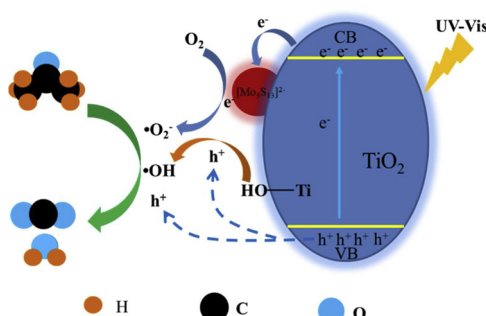


**Fig. 6.** The schematic illustration of the mineralization process of acetone under the presence of  $[Mo_3S_{13}]^{2-}/TiO_2$  composite.

the photo-induced electrons in the conduction band of  $TiO_2$  is hardly captured by intermediates such as  $O_2$ , adsorbed water, and surface hydroxyl groups, and thus it would finally recombine with holes [15].

Polypropylene non-woven fabric is the promising supporter of powder photocatalysts due to their good resistance to alkalis and acids, low cost and recyclability [32]. We loaded pristine  $TiO_2$  and  $[Mo_3S_{13}]^{2-}/TiO_2$  composite on the fabrics through spraying method (Fig. S9). The morphologies of non-woven fabrics and non-woven fabrics coated with pristine  $TiO_2$  and  $1.7[Mo_3S_{13}]^{2-}/TiO_2$  were investigated by SEM. Fig. 7(a) and (b) displayed a spatial three-dimensional structure constructed by plentiful reticular fibers, whose surface have numerous lousiness. The rough surface structure facilitated the depositing of photocatalysts. After deposition, the surface of fibers was homogeneously covered by the nanoparticles layers (Fig. 7(c) and Fig. 7(d)).

Water Contact Angle analysis were used to inquire into the surface character of the coated fabrics. The contact angle of pristine non-woven fabrics was  $132.1^\circ$  (Fig. 8(a)), which was ascribed to the hydrophobic nature of the fibers. On the contrary, the contact angle of the fabrics coated with pristine  $TiO_2$  was  $65.1^\circ$ . This phenomenon was attributed to the hydrophilic properties of  $TiO_2$  nanoparticles [52]. The fabric coated with  $1.7[Mo_3S_{13}]^{2-}/TiO_2$  composite showed the contact angle at  $117.8^\circ$ , obviously bigger than that of fabrics coated with pristine  $TiO_2$ . It has been reported that the  $[Mo_3S_{13}]^{2-}$  contained the structural motif that resembles the edge site of  $MoS_2$ , which has the hydrophobic characteristic [26,53]. Hence, this phenomenon also illustrated the

homogeneous distribution of  $[Mo_3S_{13}]^{2-}$  on the  $TiO_2$  surface.

The acetone photocatalytic degradation performance was investigated to evaluate the photocatalytic efficiency of non-woven fabrics coated with  $[Mo_3S_{13}]^{2-}/TiO_2$ . As shown in Fig. 9(a),  $CO_2$  production presented a gradually rising and stable trend along with the increasing of loading amount of  $1.7[Mo_3S_{13}]^{2-}/TiO_2$  on the fabrics. This phenomenon could be explained to that the more loading photocatalysts before it reaches the optimum loading amount ( $0.19\text{ mg}/\text{cm}^2$  in this experiment) meant the more active sites exposed to the light irradiation. The excess photocatalysts exceeding the optimum loading amount cannot further improve the mineralization of acetone. We also compared the photocatalytic mineralization activity between fabrics coated with  $[Mo_3S_{13}]^{2-}/TiO_2$  and fabrics coated with pristine  $TiO_2$  (Fig. 9(b)). The  $CO_2$  production rate for  $[Mo_3S_{13}]^{2-}/TiO_2$ -fabric was  $133.5\text{ }\mu\text{mol}/(\text{min}\cdot\text{g})$ , almost 3 times faster than that of  $TiO_2$ -fabrics ( $43.2\text{ }\mu\text{mol}/(\text{min}\cdot\text{g})$ ).

#### 4. Conclusion

In summary, non-noble metal co-catalysts  $[Mo_3S_{13}]^{2-}$  were successfully deposited on the commercial  $TiO_2$  (P25). The photocatalytic mineralization of acetone illustrated that the  $[Mo_3S_{13}]^{2-}/TiO_2$  showed greatly improved activity due to the efficient separation of photo-induced electrons and holes by  $[Mo_3S_{13}]^{2-}$ .  $[Mo_3S_{13}]^{2-}$  is even more effective than Pt as co-catalyst on promoting the photocatalytic activity. The  $[Mo_3S_{13}]^{2-}/TiO_2$  composite photocatalyst was successfully loaded on non-woven fabrics, which also showed enhanced photocatalytic mineralization activity than pristine  $TiO_2$  modified fabric. Accordingly, non-woven fabrics coated with  $[Mo_3S_{13}]^{2-}/TiO_2$  composites could be a promising photocatalytic material for indoor air purification.

#### Acknowledgments

This work is supported by National Natural Science Foundation of China (21507083, 21777097, 21777096, 21876114, 21522703), Key Laboratory of International Joint Laboratory of Resource Chemistry (IJLRC), Ministry of Education and Opening Project of Key Laboratory of Green Chemistry of Sichuan Institutes of Higher Education (LZJ1704).

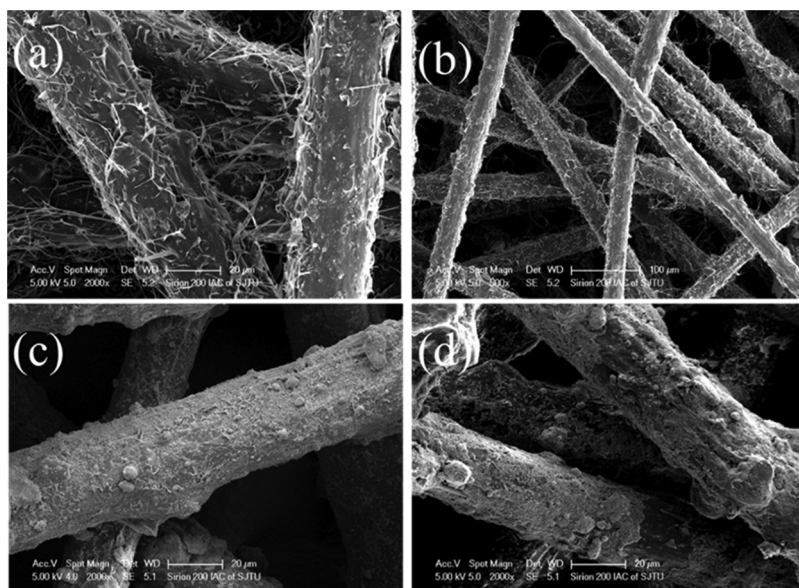


**Fig. 7.** SEM images of purified non-woven fabrics and fabrics coated with pure  $TiO_2$  and  $1.7[Mo_3S_{13}]^{2-}/TiO_2$  particles: (a) & (b) pure fabric, (c)  $TiO_2$ -fabric, (d)  $1.7[Mo_3S_{13}]^{2-}/TiO_2$ -fabric.

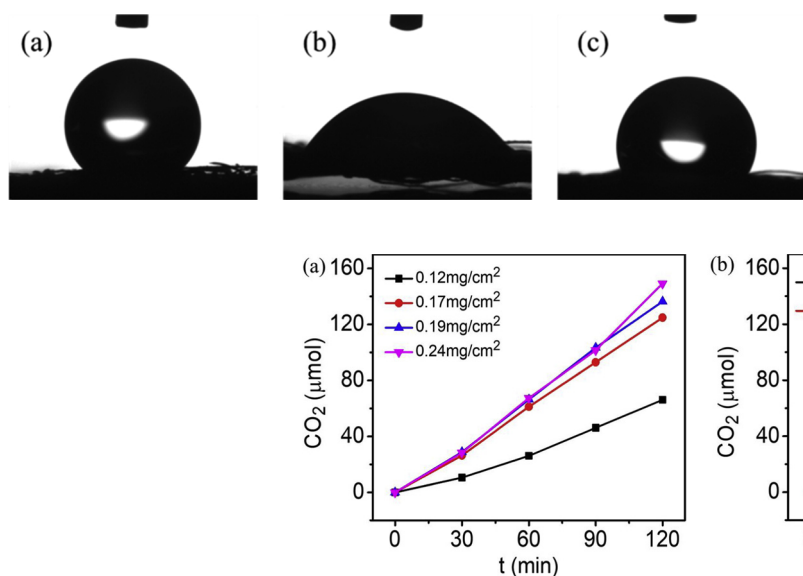


**Fig. 8.** Water droplets on different types of fabric surface: (a) pure fabric, (b) fabric coated with  $\text{TiO}_2$ , (c) fabric coated with  $1.7[\text{Mo}_3\text{S}_{13}]^{2-}/\text{TiO}_2$  composites.

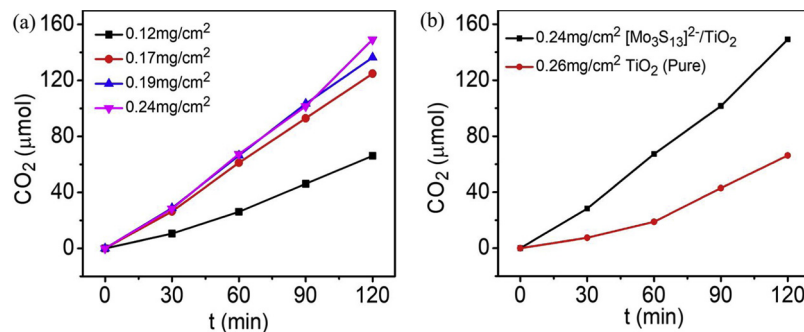


**Fig. 9.** (a)  $\text{CO}_2$  production in the presence of fabrics coated with different amounts of  $1.7[\text{Mo}_3\text{S}_{13}]^{2-}/\text{TiO}_2$  photocatalysts; (b) the comparison of  $\text{CO}_2$  production in the presence of fabrics coated with  $\text{TiO}_2$  and  $1.7[\text{Mo}_3\text{S}_{13}]^{2-}/\text{TiO}_2$  photocatalysts.

## Appendix A. Supplementary data

Supplementary material related to this article can be found, in the online version, at doi:<https://doi.org/10.1016/j.apcatb.2018.12.060>.

## References

- [1] J. Sundell, On the history of indoor air quality and health, *Indoor Air* 14 (2004) 51–58.
- [2] J. Sundell, *Indoor Environment and Health*, National Institute of Public Health, Stockholm, Sweden, 1999.
- [3] M. Li, B. Lu, Q.F. Ke, Y.J. Guo, Y.P. Guo, Synergetic effect between adsorption and photodegradation on nanostructured  $\text{TiO}_2$ /activated carbon fiber felt porous composites for toluene removal, *J. Hazard. Mater.* 333 (2017) 88–98.
- [4] X. Yan, K. Yuan, N. Lu, H. Xu, S. Zhang, N. Takeuchi, H. Kobayashi, R. Li, The interplay of sulfur doping and surface hydroxyl in band gap engineering: mesoporous sulfur-doped  $\text{TiO}_2$  coupled with magnetite as a recyclable, efficient, visible light active photocatalyst for water purification, *Appl. Catal. B* 218 (2017) 20–31.
- [5] J. Mo, Y. Zhang, Q. Xu, Y. Zhu, J.J. Lamson, R. Zhao, Determination and risk assessment of by-products resulting from photocatalytic oxidation of toluene, *Appl. Catal. B* 89 (2009) 570–576.
- [6] D. Yue, T. Zhang, M. Kan, X. Qian, Y. Zhao, Highly photocatalytic active thiomolybdate  $[\text{Mo}_3\text{S}_{13}]^{2-}$  clusters/ $\text{BiOBr}$  nanocomposite with enhanced sulfur tolerance, *Appl. Catal. B* 183 (2016) 1–7.
- [7] X. Qian, M. Ren, D. Yue, Y. Zhu, Y. Han, Z. Bian, Y. Zhao, Mesoporous  $\text{TiO}_2$  films coated on carbon foam based on waste polyurethane for enhanced photocatalytic oxidation of VOCs, *Appl. Catal. B* 212 (2017) 1–6.
- [8] Y. Boyjoo, H. Sun, J. Liu, V.K. Pareek, S. Wang, A review on photocatalysis for air treatment: from catalyst development to reactor design, *Chem. Eng. J.* 310 (2017) 537–559.
- [9] C. Pan, J. Xu, Y. Wang, D. Li, Y. Zhu, Dramatic activity of  $\text{C}_3\text{N}_4/\text{BiPO}_4$  photocatalyst with core/shell structure formed by self-assembly, *Adv. Funct. Mater.* 22 (2012) 1518–1524.
- [10] X. Zhu, S. Zhang, X. Yu, X. Zhu, C. Zheng, X. Gao, Z. Luo, K. Cen, Controllable synthesis of hierarchical  $\text{MnO}_x/\text{TiO}_2$  composite nanofibers for complete oxidation of low-concentration acetone, *J. Hazard. Mater.* 337 (2017) 105–114.
- [11] Z. Shayegan, C.S. Lee, F. Haghighat,  $\text{TiO}_2$  photocatalyst for removal of volatile organic compounds in gas phase—a review, *Chem. Eng. J.* 334 (2018) 2408–2439.
- [12] W. Lin, X. Xie, X. Wang, Y. Wang, D. Segets, J. Sun, Efficient adsorption and sustainable degradation of gaseous acetaldehyde and o-xylene using rGO- $\text{TiO}_2$  photocatalyst, *Chem. Eng. J.* 349 (2018) 708–718.
- [13] J. Wen, X. Li, W. Liu, Y. Fang, J. Xie, Y. Xu, Photocatalysis fundamentals and surface modification of  $\text{TiO}_2$  nanomaterials, *Chin. J. Catal.* 36 (2015) 2049–2070.
- [14] H. Park, Y. Park, W. Kim, W. Choi, Surface modification of  $\text{TiO}_2$  photocatalyst for environmental applications, *J. Photochem. Photobiol. C* 15 (2013) 1–20.
- [15] H. Gerischer, A. Heller, The role of oxygen in photooxidation of organic molecules on semiconductor particles, *J. Phys. Chem.* 95 (1991) 5261–5267.
- [16] C.M. Wang, A. Heller, H. Gerischer, Palladium catalysis of  $\text{O}_2$  reduction by electrons accumulated on  $\text{TiO}_2$  particles during photoassisted oxidation of organic compounds, *J. Am. Chem. Soc.* 114 (1992) 5230–5234.
- [17] X. Qian, D. Yue, Z. Tian, M. Reng, Y. Zhu, M. Kan, T. Zhang, Y. Zhao, Carbon quantum dots decorated  $\text{Bi}_2\text{WO}_6$  nanocomposite with enhanced photocatalytic oxidation activity for VOCs, *Appl. Catal. B* 193 (2016) 16–21.
- [18] J. Kim, C.W. Lee, W. Choi, Platinized  $\text{WO}_3$  as an environmental photocatalyst that generates OH radicals under visible light, *Environ. Sci. Technol.* 44 (2010) 6849–6854.
- [19] E.A. Kozlova, A.V. Vorontsov, Noble metal and sulfuric acid modified  $\text{TiO}_2$  photocatalysts: mineralization of organophosphorous compounds, *Appl. Catal. B* 63 (2006) 114–123.
- [20] H. Tada, T. Ishida, A. Takao, S. Ito, Drastic enhancement of  $\text{TiO}_2$ -photocatalyzed reduction of nitrobenzene by loading Ag clusters, *Langmuir* 20 (2004) 7898–7900.
- [21] J. Lee, W. Choi, J. Yoon, Photocatalytic degradation of N-nitrosodimethylamine: mechanism, product distribution, and  $\text{TiO}_2$  surface modification, *Environ. Sci. Technol.* 39 (2005) 6800–6807.
- [22] Q. Li, N. Zhang, Y. Yang, G. Wang, D.H.L. Ng, High efficiency photocatalysis for pollutant degradation with  $\text{MoS}_2/\text{C}_3\text{N}_4$  heterostructures, *Langmuir* 30 (2014) 8965–8972.
- [23] X. Liu, Z. Xing, Y. Zhang, Z. Li, X. Wu, S. Tan, X. Yu, Q. Zhu, W. Zhou, Fabrication of 3D flower-like black  $\text{N}-\text{TiO}_2-\text{x}/\text{MoS}_2$  for unprecedented-high visible-light-driven photocatalytic performance, *Appl. Catal. B* 201 (2017) 119–127.
- [24] Y. Yang, K. Zhang, H. Lin, X. Li, H.C. Chan, L. Yang, Q. Gao,  $\text{MoS}_2-\text{Ni}_3\text{S}_2$  heteronanorods as efficient and stable bifunctional electrocatalysts for overall water splitting, *ACS Catal.* 7 (2017) 2357–2366.
- [25] G. Ye, Y. Gong, J. Lin, B. Li, Y. He, S.T. Pantelides, W. Zhou, R. Vajtai, P.M. Ajayan, Defects engineered monolayer  $\text{MoS}_2$  for improved hydrogen evolution reaction, *Nano Lett.* 16 (2016) 1097–1103.
- [26] T.R. Hellstern, J. Kibsgaard, C. Tsai, D.W. Palm, L.A. King, F. Abild-Pedersen, T.F. Jaramillo, Investigating catalyst-support interactions to improve the hydrogen evolution reaction activity of thiomolybdate  $[\text{Mo}_3\text{S}_{13}]^{2-}$  nanoclusters, *ACS Catal.* 7 (2017) 7126–7130.
- [27] F. Guo, Y. Hou, A.M. Asiri, X. Wang, Assembly of protonated mesoporous carbon nitrides with co-catalytic  $[\text{Mo}_3\text{S}_{13}]^{2-}$  clusters for photocatalytic hydrogen production, *Chem. Commun. (Camb.)* 53 (2017) 13221–13224.
- [28] D. Yue, X. Qian, Z. Zhang, M. Kan, M. Ren, Y. Zhao, CdTe/CdS core/shell quantum dots cocatalyzed by sulfur tolerant  $[\text{Mo}_3\text{S}_{13}]^{2-}$  nanoclusters for efficient visible-light-driven hydrogen evolution, *ACS Sustain. Chem. Eng.* 4 (2016) 6653–6658.
- [29] J. Kibsgaard, T.F. Jaramillo, F. Besenbacher, Building an appropriate active-site motif into a hydrogen-evolution catalyst with thiomolybdate  $[\text{Mo}_3\text{S}_{13}]^{2-}$  clusters, *Nat. Chem.* 6 (2014) 248.
- [30] Y.Y. Lu, Y. Lin, H. Zhang, D. Ding, X. Sun, Q. Huang, L. Lin, Y.J. Chen, Y.L. Chi, S. Dong, Evaluation of volatile organic compounds and carbonyl compounds present in the cabins of newly produced, medium- and large-size coaches in China, *Int. J. Environ. Res. Publ. Health* 13 (2016).
- [31] B. Xu, Y. Wu, Y. Gong, S. Wu, X. Wu, S. Zhu, T. Liu, Investigation of volatile organic compounds exposure inside vehicle cabins in China, *Atmos. Pollut. Res.* 7 (2016) 215–220.
- [32] B. Gao, L. Liu, J. Liu, F. Yang, A photo-catalysis and rotating nano- $\text{CaCO}_3$  dynamic membrane system with  $\text{Fe-ZnIn}_2\text{S}_4$  efficiently removes halogenated compounds in water, *Appl. Catal. B* 138 (2013) 62–69.
- [33] N. Yaman, E. Özdoğan, N. Seventekein, Effect of surrounded air atmospheric plasma treatment on polypropylene dyeability using cationic dyestuffs, *Fibers Polym.* 14 (2013) 1472–1477.
- [34] K.G. Kostov, T.M.C. Nishime, L.R.O. Hein, A. Toth, Study of polypropylene surface modification by air dielectric barrier discharge operated at two different frequencies, *Surf. Coat. Technol.* 234 (2013) 60–66.
- [35] A. Falch, R.J. Kriek, Laser induced  $\text{H}_2$  production employing Pt- $\text{TiO}_2$  photocatalysts,

- J. Photochem. Photobiol. A: Chem. 271 (2013) 117–123.
- [36] Y. Sui, Q. Liu, T. Jiang, Y. Guo, One-step preparation of  $Ti^{3+}$  self-doped  $TiO_2$  single crystals with internal-pores and highly exposed {001} facets for improved photocatalytic activity, Appl. Surf. Sci. 426 (2017) 116–122.
- [37] C. Liang, P. Li, Y. Zhang, H. Gu, Q. Cai, X. Liu, J. Wang, H. Wen, G. Shao, Mild solution-processed metal-doped  $TiO_2$  compact layers for hysteresis-less and performance-enhanced perovskite solar cells, J. Power Sources 372 (2017) 235–244.
- [38] K. Du, L. Zheng, T. Wang, J. Zhuo, Z. Zhu, Y. Shao, M. Li, Electrodeposited  $Mo_3S_{13}$  films from  $(NH_4)_2Mo_3S_{13} \cdot 2H_2O$  for electrocatalysis of hydrogen evolution reaction, ACS Appl. Mater. Interfaces 9 (2017) 18675–18681.
- [39] Y. Shang, X. Xu, B. Gao, Z. Ren, Thiomolybdate  $[Mo_3S_{13}]^{2-}$  nanoclusters anchored on reduced graphene oxide-carbon nanotube aerogels for efficient electrocatalytic hydrogen evolution, ACS Sustain. Chem. Eng. 5 (2017) 8908–8917.
- [40] N.C.T. Martins, J. Ângelo, A.V. Girão, T. Trindade, L. Andrade, A. Mendes, N-doped carbon quantum dots/ $TiO_2$  composite with improved photocatalytic activity, Appl. Catal. B 193 (2016) 67–74.
- [41] S.D. Perera, R.G. Mariano, K. Vu, N. Nour, O. Seitz, Y. Chabal, K.J. Balkus, Hydrothermal synthesis of graphene- $TiO_2$  nanotube composites with enhanced photocatalytic activity, ACS Catal. 2 (2012) 949–956.
- [42] F. Guo, Y. Hou, A.M. Asiri, X. Wang, Assembly of protonated mesoporous carbon nitride with co-catalytic  $[Mo_3S_{13}]^{2-}$  clusters for photocatalytic hydrogen production, Chem. Commun. (Camb.) 53 (2017) 13221–13224.
- [43] J. Kibsgaard, T.F. Jaramillo, F. Besenbacher, Building an appropriate active-site motif into a hydrogen-evolution catalyst with thiomolybdate  $[Mo_3S_{13}]^{2-}$  clusters, Nat. Chem. 6 (2014) 248–253.
- [44] D. Yue, Z. Zhang, Z. Tian, T. Zhang, M. Kan, X. Qian, Y. Zhao, Highly photocatalytic active thiomolybdate  $[Mo_3S_{13}]^{2-}$  clusters/ $Bi_2WO_6$  nanocomposites, Catal. Today 274 (2016) 22–27.
- [45] K. Chen, L. Zhu, K. Yang, Tricrystalline  $TiO_2$  with enhanced photocatalytic activity and durability for removing volatile organic compounds from indoor air, J. Environ. Sci. 32 (2015) 189–195.
- [46] Q. Sun, Hui Li, S. Zheng, Z. Sun, Characterizations of nano- $TiO_2$ /diatomite composites and their photocatalytic reduction of aqueous Cr (VI), Appl. Surf. Sci. 311 (2014) 369–376.
- [47] Y. Zou, J. Shi, D. Ma, Z. Fan, L. Lu, C. Niu, In situ synthesis of C-doped  $TiO_2@C_3N_4$  core-shell hollow nanospheres with enhanced visible-light photocatalytic activity for  $H_2$  evolution, Chem. Eng. J. 322 (2017) 435–444.
- [48] C.L. Bianchi, S. Gatto, C. Pirola, A. Naldoni, A. Di Michele, G. Cerrato, V. Crocellà, V. Capucci, Photocatalytic degradation of acetone, acetaldehyde and toluene in gas-phase: comparison between nano and micro-sized  $TiO_2$ , Appl. Catal. B 146 (2014) 123–130.
- [49] S. Hwang, M.C. Lee, W. Choi, Highly enhanced photocatalytic oxidation of CO on titania deposited with Pt nanoparticles: kinetics and mechanism, Appl. Catal. B 46 (2003) 49–63.
- [50] A.H. Mamaghani, F. Haghigat, C.-S. Lee, Photocatalytic oxidation technology for indoor environment air purification: the state-of-the-art, Appl. Catal. B 203 (2017) 247–269.
- [51] T. Fotiou, T.M. Triantis, T. Kaloudis, K.E. O'Shea, D.D. Dionysiou, A. Hiskia, Assessment of the roles of reactive oxygen species in the UV and visible light photocatalytic degradation of cyanotoxins and water taste and odor compounds using C- $TiO_2$ , Water Res. 90 (2016) 52–61.
- [52] K. Liu, M. Cao, A. Fujishima, L. Jiang, Bio-inspired titanium dioxide materials with special wettability and their applications, Chem. Rev. 114 (2014) 10044–10094.
- [53] J. Lee, P. Dak, Y. Lee, H. Park, W. Choi, M.A. Alam, S. Kim, Two-dimensional layered  $MoS_2$  biosensors enable highly sensitive detection of biomolecules, Sci. Rep. 4 (2014) 7352.